EXAFS Measurements of Quasi-Isentropically Compressed Vanadium Targets on the OMEGA Laser

Introduction

The response of materials to shocks and other high-strain-rate deformation is the subject of intense research.[1] There is particular interest in developing and testing constitutive models that allow continuum hydrodynamic computer codes to simulate plastic flow in the solid state. Such models are important for the study of material strength under high-strain and high-strain-rate conditions. To test such models, the conditions within the compressed samples (such as compression and temperature) must be measured on a nanosecond time scale. We describe experiments on the OMEGA[2] laser where vanadium (V) is compressed quasi-isentropically to a pressure of ~0.75 Mbar and its compression and temperature are measured by Extended X-Ray Absorption Fine Structure (EXAFS).[3] Isentropic compression (where the entropy is kept constant) enables us to reach high compressions at relatively low temperatures. This is important for the study of highly compressed metals at temperatures well below the melting point. Additionally, significant EXAFS modulations can be obtained only at sufficiently low temperatures. The study of deformations and crystal phase transformations of compressed metals requires that the temperature be kept below melting. This limits the pressure that can be applied in shock compression. Examining the Hugoniot curve that describes the trajectory of shocks in parameter space shows that vanadium will melt[4] at a pressure of ~2.4 Mbar (and a temperature of ~8000 K), precluding solid-state studies at higher pressures. However, quasi-isentropic compression experiments (ICE), involving a slower-rising compression, can access much higher pressures and still stay below the melting curve. Laser-driven quasi-isentropic compression can be achieved by a two-stage target design[5] where a laser of a few-nanosecond pulse irradiates a "reservoir" layer. When the laser-generated shock wave reaches the back of the reservoir, the material releases and flows across a vacuum gap and stagnates against the sample ("plasma impact"), causing its pressure to rise over a period of a few tens of nanoseconds. This configuration has been previously studied and pressures of up to 2 Mbar demonstrated.[6–8] The main diagnostic in those experiments was the interferometric measurement of the back target surface, which, when back-integrated (in time and space), can yield the

pressure on the front surface as a function of time. EXAFS has the unique advantage of yielding information on the sample temperature. This is particularly important to measure because the stagnating reservoir material causes severe heating of the front sample surface, unless protected by a heat shield. The ability to measure temperatures of the order of 10^3 K is unique to EXAFS, as is the ability to *directly* measure compression and temperature within the sample. The EXAFS results show details not seen in the VISAR results: without the use of a heat shield, the heating of the target leads to a lower compression. Also, higher laser intensities can lead to nonuniformities due probably to hydrodynamic instability.

The use of *in-situ* EXAFS for characterizing nanosecond laser–shocked vanadium, titanium, and iron has been recently demonstrated.[9,10] Additionally, the observed EXAFS was shown to indicate crystal phase transformation due to shock compression: the α-to-ω transformation in titanium[9] and the body-centered-cubic (bcc) to hexagonal-closely-packed (hcp) phase transformation in iron.[10] We show here that EXAFS can likewise be applied to the case of laser-driven, quasi-isentropic compression experiments (ICE).

EXAFS modulations above an absorption edge are due to the interference of the ejected photoelectron wave with the reflected wave from neighboring atoms.[3] This interference translates into modulations in the cross section for photon absorption above the K edge, the measured quantity. The frequency of these modulations relates to the interparticle distance, hence the density of the compressed material. The decay rate of the modulation with increasing photoelectron energy yields the mean-square relative displacement (σ) of the crystal atoms and serves as a temperature diagnostic. The basic theory of EXAFS[3] yields an expression for the relative absorption $\chi(k) = \mu(k)/\mu_0(k) - 1$, where $\mu(k)$ is the absorption coefficient and $\mu_0(k)$ is the absorption of the isolated atom. The wave number k of the ejected photoelectron is given by the de Broglie relation $\hbar^2 k^2/2m = E - E_K$, where E is the absorbed photon energy and E_K is the energy of the K edge. The measured spectrum yields the absorption $\mu(E)$, which is converted

to $\chi(k)$. The derived $\chi(k)$ is analyzed with the FEFF *ab initio* EXAFS software package.[11] The basic EXAFS formula for a single reflection in the plane-wave approximation is[3]

$$\chi(k) = \sum_j N_j S_0^2 F_j(k) \exp\left[-2\sigma^2 k^2 - 2R_j/\lambda(k)\right]$$

$$\times \sin\left[2kR_j + \phi_j(k)\right]/kR_j^2, \tag{1}$$

where N_j is the number of atoms in the j-th shell, that is, the number of atoms surrounding the absorbing atom at a distance R_j, and $\lambda(k)$ is the mean free path for collisions. FEFF uses the scattering potential to calculate the amplitude and phase shift of the photoelectron waves scattered from several shells of neighboring atoms including multiple scattering paths. The total $\chi(k)$ is constructed in the curved-wave approximation (i.e., the assumption of plane wave is removed) and iteratively fitted to the experimental $\chi(k)$. The main fitting parameters are the nearest-neighbor distance R and the vibration amplitude σ^2 appearing in the Debye–Waller term. R yields the density or compression; since R is the frequency of the modulations in k space, a compression results in the lengthening of the period of EXAFS modulations (a similar lengthening will also be evident in the photon-energy space, i.e., in the original spectrum). As a function of temperature, σ^2 was calculated using the Debye model[12] for the phonon density of states, including correlation, and it also depends on the density through the Debye temperature. Using the density dependence[13] of the Debye temperature for V and the result for σ^2 from the FEFF fitting, the temperature can be derived. As the temperature increases, the EXAFS oscillations decay faster with increasing photon energy (or increasing electron wave number).

The use of EXAFS for diagnosing compressed metals places a severe restriction on the temperature since at higher temperatures the damping of the EXAFS modulations (because of an increase in σ^2) may preclude reliable measurement. A useful general criterion for the observation of significant EXAFS modulations is the requirement for σ^2 to not exceed ~0.015 Å^2. The averaged square vibration amplitude σ^2 increases with the temperature, but compression mitigates this increase because the Debye temperature increases with density. At normal density the temperature T_0 of vanadium at which $\sigma^2 = 0.015$ Å^2 is $T_0 \sim 500$ K, whereas at a compression of 1.5 that temperature increases to $T_0 \sim 1800$ K. Thus, compression extends the range of temperatures where EXAFS can be observed. This compression, when achieved by a shock [at a pressure of ~1.8 Mbar (Ref. 14)], will result in a temperature of ~5000 K, much higher

than T_0. Thus, in spite of the compression, significant EXAFS modulations would not be visible in that case. On the other hand, an examination of the equation of state of vanadium[15] shows that in a purely isentropic compression, the temperature corresponding to 1.8 Mbar will rise to only ~530 K. Thus, in future ICE experiments, even if not purely isentropic, EXAFS could be measured at pressures of several Mbar and possibly higher.

The drive (i.e., the pressure as a function of time at the front surface of the sample) is calibrated by substituting aluminum for the vanadium; this pressure is independent of the material of the sample. The drive pressure is deduced, for various laser intensities, by interferometrically measuring the velocity of the back target surface (VISAR[16]) as a function of time and then integrating it backward in time and space to obtain the drive.[17] Aluminum is used because its equation of state is well known, and LiF is used because it is transparent to the VISAR laser and its acoustical impedance is well matched to that of aluminum, minimizing reflections at the interface. The behavior of the total target (reservoir, vacuum gap, and sample) is simulated by the hydrodynamic code *LASNEX*.[18] The code results are compared with both the measured back-surface velocity as well as the drive pressure obtained as explained above. Good agreement validates the use of such simulations for the case of the vanadium sample. The *LASNEX*-simulated compression and temperature within the vanadium can be compared with the EXAFS results.

In addition to the inevitable heating due to the compression, there are three sources of extraneous heating (called here preheat): (a) radiation from the imploding target (the radiation source, or the backlighter), (b) radiation from the laser-drive absorption region, and (c) heat generated from the plasma impact upon stagnation and conducted into the sample. The first preheating occurs during the EXAFS probing, whereas the other two occur before the onset of sample compression. Ways to measure as well as to minimize these heating sources are described below.

The present work demonstrates the feasibility and finds the limitations of laser-driven quasi-isentropic compression experiments, rather than carrying out a systematic parameter study. Typical results will highlight these limitations.

The following sections of this article (1) explain the experimental setup and procedures; (2) present the VISAR results and their analysis; (3) present the special case of high-irradiance, which leads to nonuniform compression; (4) analyze the role of the heat shield; (5) discuss the measurement of preheat;

and (6) present the EXAFS measurements of compression and heating.

Experimental

Figure 111.31 shows a schematic of the experimental configuration used to measure K-edge EXAFS absorption spectra. The target consisted of two parts: a reservoir and a sample (V or Al), separated by a vacuum gap of either 300 or 400 μm. The reservoir includes an undoped, 125-μm-thick polyimide layer and a 50-μm-thick CH layer, doped with 2% (by number of atoms) of bromine. The bromine minimizes the sample heating by radiation from the laser-absorption region. The doping is limited to only the back of the reservoir to prevent laser heating of the doped layer, which would have increased the emitted radiation, and thus the preheating. The doping concentration is limited to minimize the absorption of source radiation within the reservoir, which reduces the intensity available for the EXAFS measurement. The sample (10-μm-thick polycrystalline V) was coated on the laser side with 8 μm of a low-conduction parylene-N heat shield. Its role is to protect the sample from heat conducted from its surface, where the reservoir plasma impact occurs. On some of the shots the heat shield was absent in order to demonstrate its effect. The V sample was backed by a 500-μm-thick C_2H_4 substrate, which served to minimize sample heating by the soft radiation from the imploding EXAFS source. This radiation shield also prevents rarefaction of the sample when the pressure wave arrives at its rear surface. The thickness of the radiation shield was chosen to heavily absorb the radiation below the vanadium K edge (5.463 keV) while absorbing only slightly the radiation above the K edge, where the EXAFS modulations occur. To further minimize this preheat, the target-backlighter distance (19 mm) was the largest possible on OMEGA. As explained before, in the VISAR drive-calibration shots, the V was replaced by Al and the radiation shield was changed to LiF. The rest of the targets were identical to that with the vanadium sample. For the calibration shots there is no backlighter and the VISAR laser travels from the right in Fig. 111.31.

Eleven driving laser beams, 3-ns square pulse each, were fired simultaneously and focused to an ~3-mm focal spot, yielding an irradiance of ~17 TW/cm^2 (some results for different irradiances are mentioned below). The x-ray spectrum is obtained when a fan of rays originating at the backlighter fall on the flat crystal at different Bragg angles, reflecting a slightly different wavelength at each point. The spectral range of the EXAFS spectrum (~5.5 to 6 keV) subtends a distance of ~0.5 mm at the target. A 3-mm-focal-spot size was chosen so that the EXAFS rays probe a small central region of the focal spot. This necessitates working without distributed phase plates (DPP's),[19] which create intensity nonuniformity in the focal spot. Some of this nonuniformity is smoothed out when the reservoir material flows across the vacuum gap (as will be shown in Fig. 111.33) for the uniformity of the back-surface motion. Specially designed phase plates for an ~3-mm focal-spot size could improve the quality of these experiments. The spectral resolution (limited by the size of the imploded backlighter core) is ~10 eV, much smaller than a typical EXAFS modulation period.
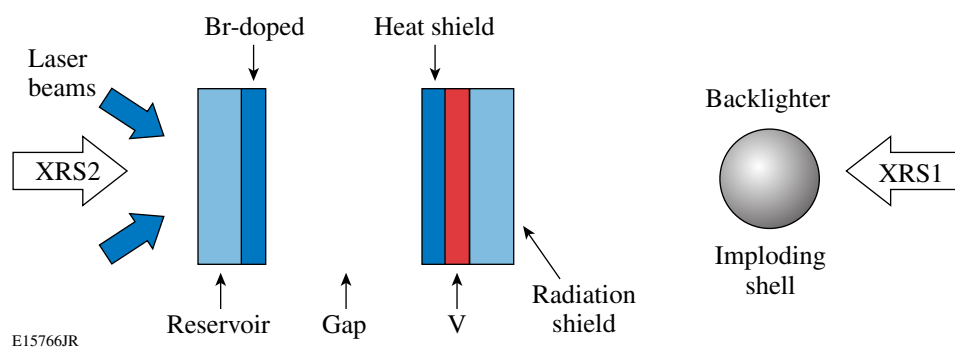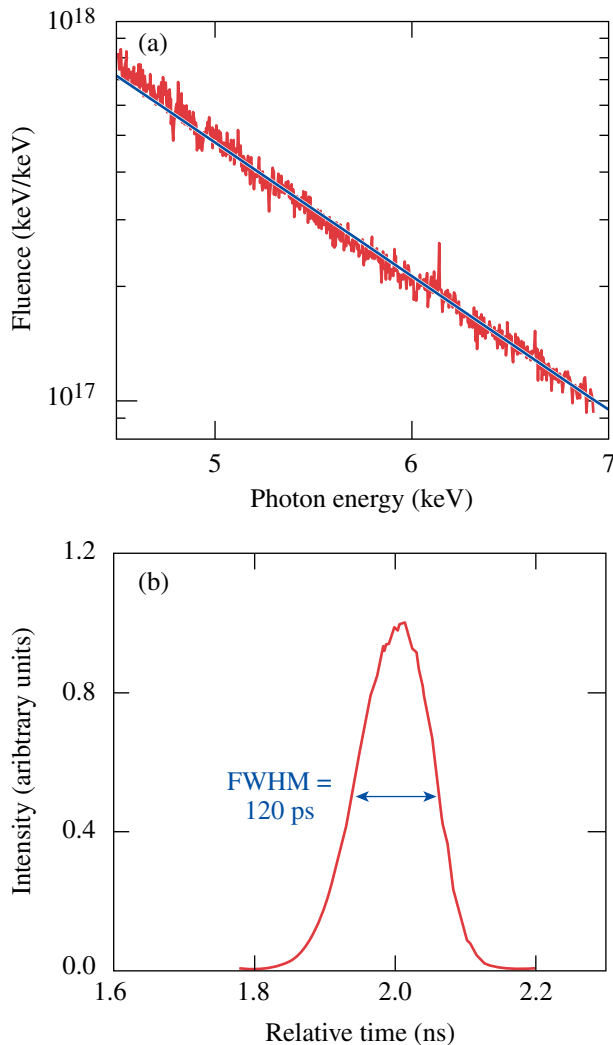

Figure 111.31
Schematic of the experimental configuration for EXAFS measurement of ICE targets. For calibrating the drive, the V is replaced by Al and the radiation shield by LiF, the backlighter is removed, and the VISAR laser travels from right to left. XRS1 and XRS2 are x-ray spectrometers that measure, respectively, the incident and transmitted spectra. The Br doping reduces heating due to radiation from the laser-deposition region, the heat shield reduces heating due to the impact of reservoir material on the sample, and the radiation shield reduces heating due to the backlighter.

The backlighter is formed by focusing 40 of the OMEGA beams on a CH shell of ~16-μm thickness and ~850-μm outer diameter, filled with 0.1 atm of argon, using a 1-ns square pulse. At peak compression the compressed core of the target (<100 μm in size) emits an intense continuum that is spectrally smooth [see Fig. 111.32(a)]; this is a requisite for measuring the inherently weak modulations in the absorption spectrum. Two cross-calibrated, flat-crystal spectrometers equipped with a Ge (1,1,1) crystal were placed at the extreme right and left positions in Fig. 111.31. The first was used to measure the inci-

dent spectrum (I_0) and the second to measure the transmitted spectrum (I). The absorption as a function of photon energy E is defined as $\mu(E) = \ln\left[I_0(E)/I(E)\right]$. I_0 has to be corrected for the (known) absorption of backlighter radiation in the radiation shield. Absorption of the transmitted radiation (I) in the reservoir is small, and, additionally, at the time of EXAFS probing, most of the reservoir material has been ablated away. The measured intensity also includes radiation from the laser-deposition region, which is subtracted. To measure this contribution (typically, ~10% of the total), we fire the drive beams without irradiating the backlighter. A final adjustment of I_0/I can be done far above the K edge, where EXAFS modulations are heavily damped and the absorption $\mu_0(E)$ is well known. The delay time of the drive beams with respect to the back-lighter beams was varied so that the EXAFS could probe the vanadium at different times during the compression. Although the spectrometers used in the EXAFS measurement are time integrated, a meaningful shock diagnosis can be obtained without streaking the spectrum in time because the x-ray pulse width [Fig. 111.32(b)] is only ~120 ps, much shorter than the compression-wave transit time through the metal (~20 ns).

Results and Analysis

1. VISAR Results

Figure 111.33 shows a typical VISAR record for the case of an ICE target without a heat shield, driven at 17 TW/cm^2. The time refers to the delay with respect to firing the drive-laser beams; a timing fiducial is shown above the VISAR record. The
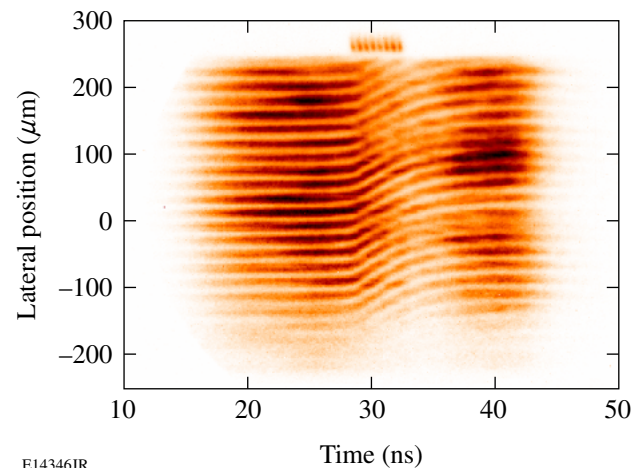

E12438JR

Figure 111.32
(a) Typical spectrum emitted by the backlighter, used as a source for the measurement of absorption above the vanadium K-shell edge at 5.46 keV. The use of imploding CH shells creates a continuum without spectral lines, essential for reliable EXAFS measurements. (b) Streaked x-ray emission from the imploding backlighter target. Radiation above ~3 keV is emitted during peak compression (earlier emission is negligibly small), ensuring a short x-ray probing pulse.

E14346JR

Figure 111.33
VISAR record for the case of an ICE target without a heat shield, driven at 17 TW/cm^2. The time refers to the delay with respect to firing the drive-laser beams; a timing fiducial is shown above the VISAR record. The fringe motion tracks the Al particle motion at the reflective Al–LiF interface. The smooth, gradual fringe shift with time is indicative of shockless, quasi-isentropic compression.

fringes are produced by the interference of the VISAR laser with the beam reflected from the back surface of the target. The vertical displacement of fringes is proportional to the Al particle velocity at the Al–LiF interface. The velocity results reported here refer to a spatial average over the 150-μm central portion of the field of view. The smooth, gradual fringe shift with time indicates shockless, quasi-isentropic compression. The relative uniformity (or planarity) of the drive is evidenced by the quasi-simultaneous arrival of the pressure wave (at ~30 ns) and the small variations (±10%) in the slope of the fringes (i.e., the acceleration). This uniformity is achieved even though no smoothing was applied to the incident laser beams; nonuniformities in the laser irradiation are smoothed during the propagation through the target vacuum gap, leading to a more-uniform back-surface velocity.

The analysis of VISAR records, such as that in Fig. 111.33, proceeds in two directions: by back-integrating the VISAR-measured velocity and by comparing with 1-D simulations of the *LASNEX* code. Normally, the back-surface velocity is used to derive the front-surface pressure, which is then used as input to a hydrodynamic code. The code then simulates the forward propagation whose end result is the back-surface velocity. This derived velocity is, in turn, compared with the measured velocity. This procedure cannot yield any information on the heating due to the three preheat sources mentioned above. *LASNEX* is used to simulate the entire experiment, starting with the laser interaction, the reservoir expansion, and the sample compression. Because of the resulting complexity, the application of *LASNEX* requires some adjustments to fit the data. This is thought to be due to 2-D effects that are neglected in these 1-D runs (primarily related to the nonuniformities of the unsmoothed beams) as well as uncertainties in the equation of state of the expanding reservoir plasma. Our confidence in the validity of the simulations depends on their agreement with both the measured back-surface velocity as well as the deduced front-surface pressure. Additionally, the code simulations are compared with the EXAFS results.

A sample of such an analysis of VISAR results (Fig. 111.34) shows the rear-surface velocity (upper frames) and the drive pressure (lower frames) for three different cases: irradiance of (a) 17 TW/cm^2, (b) 17 TW/cm^2 with no Br in the ablator, and (c) 10 TW/cm^2. In (a) and (c) the reservoir contained a brominated layer; in (b) the brominated layer was replaced with an equal-thickness CH layer. The vacuum gap was 400 μm. The solid curves show simulation results by the *LASNEX* code; the dashed curves show experimental results. The dashed velocity curves are directly from the VISAR-measured results; the
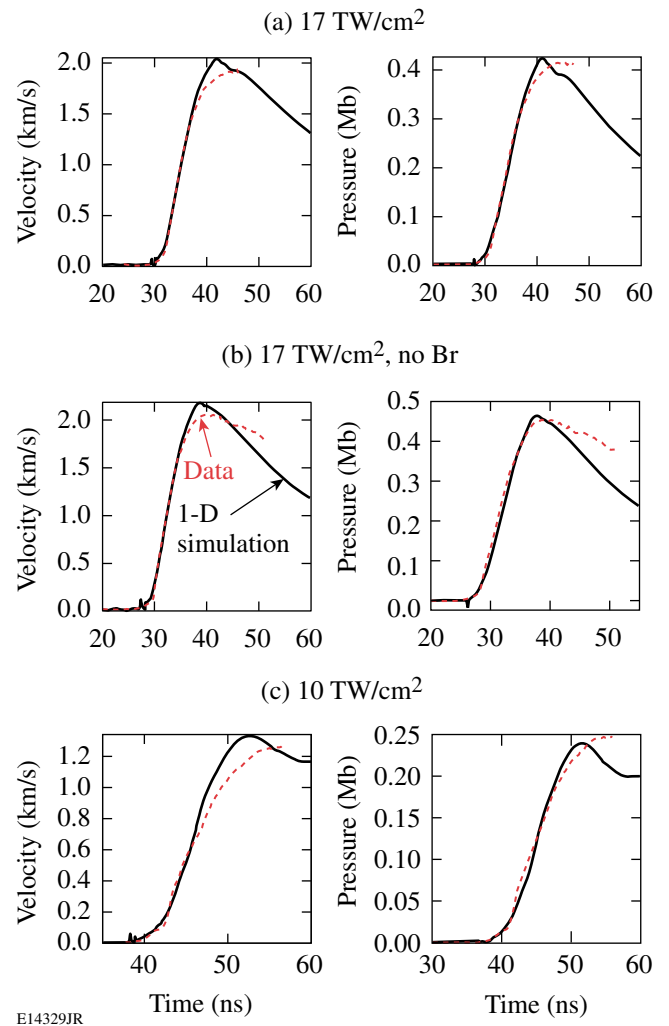

(a) 17 TW/cm^2

(b) 17 TW/cm^2, no Br

(c) 10 TW/cm^2

E14329JR

Time (ns)

Figure 111.34
Rear-surface velocity (left column) and drive pressure (right column) for three different cases: irradiance of (a) 17 TW/cm^2, (b) 17 TW/cm^2 (no Br), and (c) 10 TW/cm^2. The solid curves show simulation results by the *LASNEX* code. The dashed velocity curves (upper) show the VISAR-measured results; the dashed pressure curves (lower) are obtained from the measured velocity curves by back-integration. The rise in velocity and pressure is seen to be slow and smooth, characteristic of shockless compression.

dashed pressure curves are obtained from the measured velocity curves by back-integration.[17] A heat shield was not used in any of these cases. The rise in velocity and pressure is seen to be slow and smooth, characteristic of shockless compression. The small differences between the code and experimental results around peak compression and later are not well understood; similar disagreements with 1-D simulations were also observed in ICE results reported in Fig. 7(b) of Ref. 5. To obtain the velocity fits in Fig. 111.34, two small adjustments had to be introduced in the *LASNEX* runs (no additional adjustments

had to be made to fit the pressure curves): (a) the assumed laser power had to be reduced by ~30% from the measured values to fit the magnitude of the velocity curve; this is due to the reduction in absorption due to the oblique incidence of the laser beams, and (b) the time scale had to be shifted by a few nanoseconds to fit the time of peak velocity. Nevertheless, the code simulations provide strong support for the VISAR measurements of velocity and pressure as well as the compression and temperature measurements by EXAFS. This is because the main interest here is understanding the sample compression, whereas the interaction of the laser with the reservoir is of secondary importance. Figure 111.34 shows that the inclusion of Br doping slightly reduces the pressure achieved. Examination of the simulations shows that this is caused by the weakening of the compression pressure: the shock traveling within the reservoir weakens when passing from the polyimide to the less-dense CH(Br) layer, then further weakens when traveling through the latter layer. Thus, the total weakening is higher for a thicker CH(Br) layer.

2. High-Irradiance Target Experiments

The laser irradiance for most of the target experiments described in this article was 17 TW/cm^2 for which the achieved pressure was ~0.4 Mbar (see Fig. 111.34). At the higher irradiance of 25 TW/cm^2, the VISAR results indicate a pressure of 0.75 Mbar. However, significant target nonuniformities are indicated in the EXAFS record, at irradiances above ~22 TW/cm^2. This precludes meaningful EXAFS analysis. Figure 111.35(a) shows the VISAR-measured velocity and the deduced pressure evolution for a 400-μm-vacuum-gap target, without a heat shield, and a laser irradiance of 25 TW/cm^2. Figure 111.35(b) shows the EXAFS record for a target experiment at the same conditions. The horizontal axis corresponds to the dispersed photon energies (the K edge is seen at 5.46 keV), whereas the vertical axis corresponds to a one-dimensional image (or face-on radiograph) of the vanadium layer. The energy range shown (~5.4 to 5.8 keV) is where the EXAFS modulations are normally seen. The horizontal axis also corresponds to a face-on radiograph of the vanadium sample, except that at each horizontal position, a different photon energy contributes to the image. Thus, Fig. 111.35(b) is a quasi-2-D face-on radiograph of the vanadium. The relative modulation depth of the structures is ~15% (corresponding to vanadium thickness modulation of ± 0.5 μm), considerably higher than the modulation depth of the expected EXAFS (<5%), making the reliable measurement of EXAFS impossible. It should be noted that the EXAFS modulations [appearing as vertical lines in records like that in Fig. 111.35(b)] are due to modulations in the absorption as functions of photon energy, whereas the 2-D structure modulations

(a)

(b)
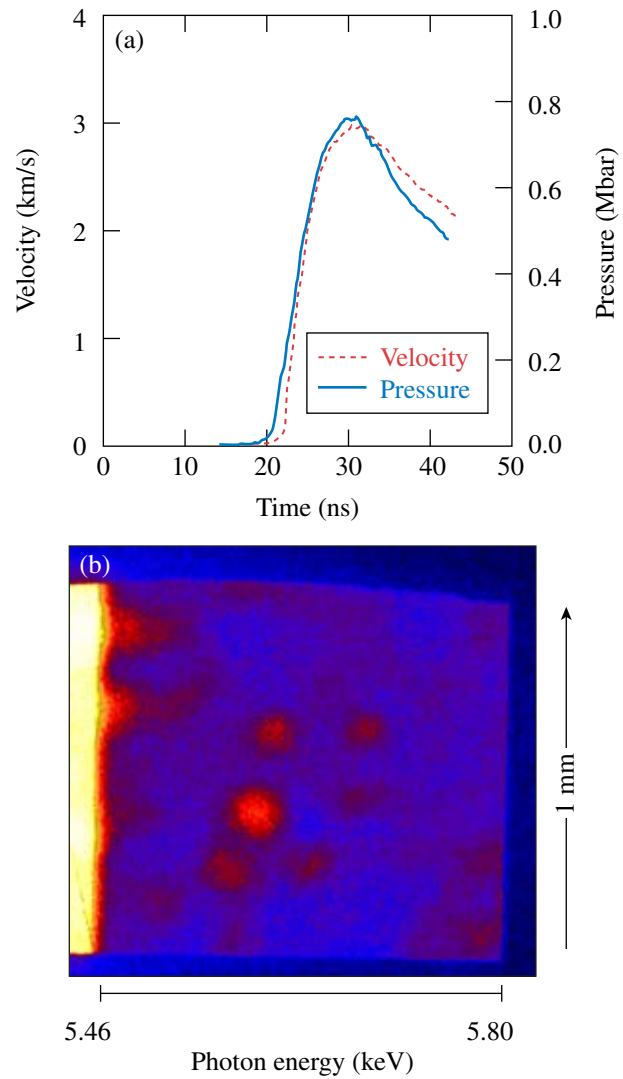
E15767JR

Figure 111.35
(a) High pressure achieved with high laser irradiance: VISAR-measured back-surface velocity and derived pressure for an irradiance of 25 TW/cm^2 (400-μm-vacuum-gap target, without a heat shield). (b) EXAFS record for a target shot at this irradiance showing nonuniformities believed to be due to the instability of the rarefaction wave following the unloading of the laser-launched shock at the rear surface of the reservoir. (The EXAFS record is effectively a 2-D radiograph of the target, and the intensity modulations are due to modulations in the thickness of the vanadium layer.)

in Fig. 111.35(b) must be due to modulations in the thickness of the vanadium layer. Similar behavior was seen for targets with or without a heat shield. A possible explanation for this observed modulation is related to the instability occurring when the laser-launched shock arrives at the back surface of the reservoir, leading to a rarefaction wave moving in the opposite direction.[20] Modulations in the density of the expanding reservoir material grow linearly with time, at a rate proportional to

the shock speed and the perturbation wave number (see Fig. 5 in Ref. 20). These modulations result in modulations in the strength of impact on the target and, therefore, to modulations in the latter's compression. The instability appears for targets with or without a heat shield. The only common characteristic of the unstable cases is the high laser irradiance. This can be explained by the higher shock speed at higher laser intensities, leading to a higher growth rate. It is noteworthy that these nonuniformities do not seem to affect the VISAR signal [Fig. 111.35(a)]. The remainder of this article shows only results at irradiances lower than 20 TW/cm^2, where the nonuniformities discussed here were not observed.

3. The Heat Shield

Simulations described below show that without a heat shield, the front surface of the sample heats up substantially (>10^4 K for 17 TW/cm^2) and the heat flow into the sample creates a temperature gradient. The inclusion of a heat shield greatly reduces this heating and creates a quasi-uniform temperature profile of the order of 10^2 K. This heating has a dramatic effect on the EXAFS spectra, as seen when comparing EXAFS results for the two cases of targets with and without a heat shield. As explained above, EXAFS is sensitive to the temperature because of the Debye–Waller term in Eq. (1). The back-surface velocity (both measured and simulated) is affected very little by this heating. This is related to the fact that the pressure in the sample is determined mainly by the reservoir plasma at stagnation and the effect of target preheat is mainly to lower the density; in the relevant part of parameter space a very large increase in temperature at a constant pressure causes only a small decrease in density. Therefore, to achieve maximum compression and uniform, low temperature in laser ICE experiments, it is necessary to use targets with a heat shield.

The effect of the heat shield on the target behavior was studied with 1-D runs of the *LASNEX* code. Figure 111.36(a) shows the evolution of pressure on the front surface of the vanadium sample, with and without a heat shield, for otherwise identical conditions. Dashed curves refer to targets with a heat shield; solid curves refer to targets without a heat shield. In Fig. 111.36(b), the curves that rise later correspond to the 400-μm vacuum gaps. The smaller vacuum gap yields a higher pressure. The introduction of a heat shield creates a weak shock, as evidenced by the sharp initial rise in pressure. Some reverberation is due to shock reflections, but when the pressure increases further, its behavior is almost the same as when the heat shield is absent. The predicted effect of the heat shield on the rear-surface velocity is seen in the experiment (Fig. 111.33 compared with Fig. 111.37 below). Figure 111.36(b) shows the
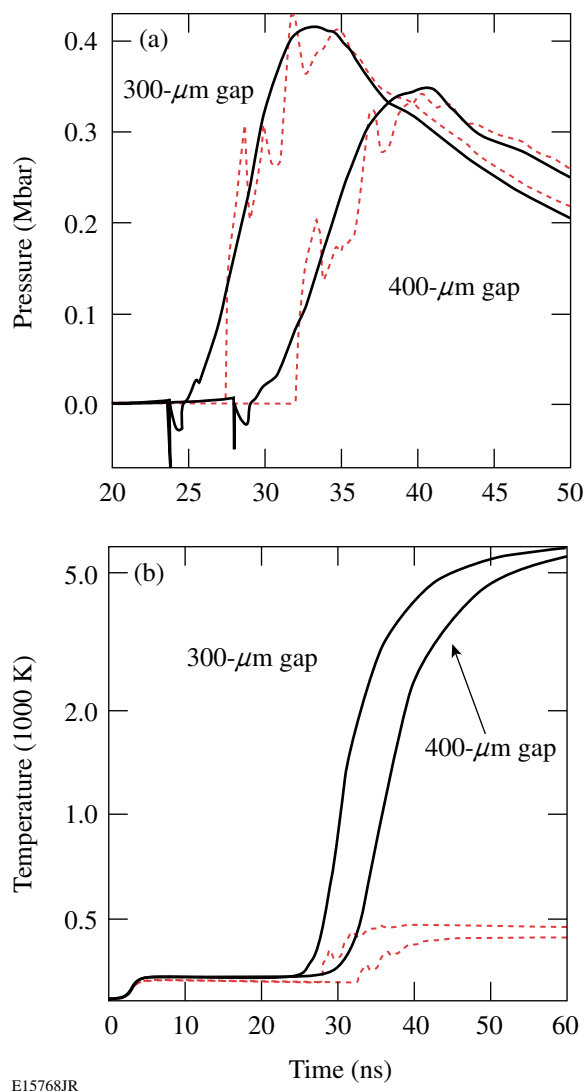

Figure 111.36
LASNEX simulation for targets of two different vacuum gaps, with and without a heat shield: (a) the evolution of pressure on the front surface of the vanadium sample, and (b) the evolution of temperature in the middle of the vanadium sample. Dashed curves: with a heat shield; solid curves: without a heat shield. The heat shield is seen to effectively block the heating from reaching the sample. It has a much greater effect on the temperature than on the pressure. The results in (a) are borne out by the VISAR results and those in (b) by the EXAFS results.

evolution of temperature in the middle of the vanadium sample with and without a heat shield. The heat shield effectively eliminates the heat flow from the front surface. More simulation examples, as will be shown in Figs. 111.42 and 111.43, can be summarized as follows (for 17 TW/cm^2 at times ≥35 ns): (a) With a heat shield the temperature is quasi-uniform and low (~10^2 K) and the compression is 15%. (b) Without a heat shield the temperature falls sharply from a very high surface value

($>10^4$ K) and toward the back surface approaches ~500 K. The compression, ~8%, is much smaller than with a heat shield. These simulation results are borne out by the EXAFS measurements (as will be shown in Fig. 111.43).

Figure 111.37 shows the VISAR-measured rear-surface velocity of an ICE target of 300-μm vacuum gap, with a heat shield, irradiated at 20 TW/cm^2. In close agreement with Fig. 111.36, the heat shield introduces a sharp initial rise in the velocity due to a shock, but later the velocity approaches a curve characteristic of a shockless compression. Thus, the employment of a heat shield results in a significant improvement in target performance, with only a small perturbation. The thickness of the heat shield (8 μm) was chosen to be sufficiently large to protect the sample from heating but not large enough to cause steepening of the compression wave into a strong shock. With Be, where both the density and the sound speed are higher than for CH, a thicker heat shield could be used without causing such steepening.
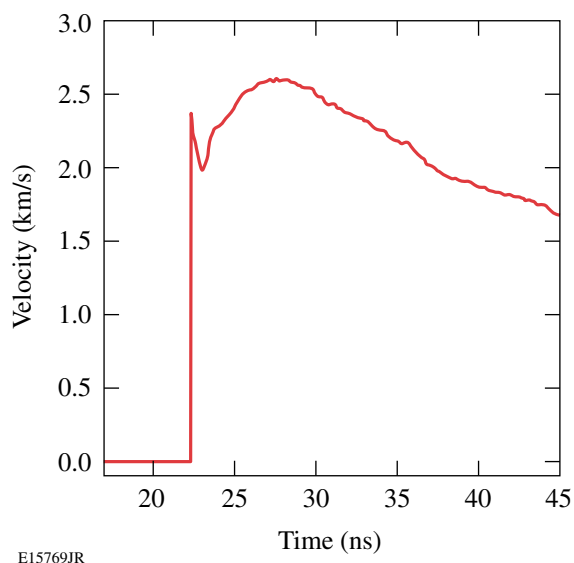

E15769JR

Figure 111.37
VISAR-measured rear-surface velocity of an ICE target of 300-μm vacuum gap, with a heat shield, irradiated at 20 TW/cm^2. In close agreement with Fig. 111.36, the heat shield introduces a sharp initial rise in the velocity due to a shock, but later the velocity approaches the shape of the velocity curve obtained with no heat shield.

4. Measurements of Preheat

To measure the temperature rise due to backlighter radiation, the EXAFS spectrum is obtained when irradiating the backlighter but without firing the drive beams. The temperature rise deduced from the EXAFS spectrum is then solely due to the backlighter radiation. The temperature is deduced from a

fit of the EXAFS spectrum calculated by the FEFF code to the experimental spectrum. As explained in the **Introduction** (p. 167), the parameters R (nearest-neighbor distance) and σ (mean atomic vibration amplitude) in the FEFF code are varied to yield the best fit. The resulting values of R and σ yield the temperature and compression. A typical result is shown in Fig. 111.38. Here the best fit of the FEFF code corresponds to a compression of 1 (i.e., the normal density of vanadium, 6.11 g/cm^3) and a temperature rise from room temperature of $\Delta T \sim 200$ K. The precision of temperature determination[8] is 10% to 15%.

To measure the preheat by radiation from the laser-deposition region, the target is probed at ~20 ns after firing the driving beams, i.e., before the impact of the expanding reservoir on the vanadium sample. The FEFF fit shown in Fig. 111.39 yields a temperature of 630 K (and normal density). Of this, a rise of ~200 K is shown in Fig. 111.38 to be due to the backlighter radiation. Thus, the temperature rise due to radiation from the laser-deposition region is ~130 K. The corresponding calculated preheat can be read off Fig. 111.36(b) at times <30 ns (preheat due to the backlighter is not included in the simulations). The result is ~90 K; the discrepancy could be due to shot irreproducibility (since two target experiments are required to make this determination). It should be noted that heating due to radiation from the laser-deposition region in the case of shock compression[8,9] is negligible because in that case
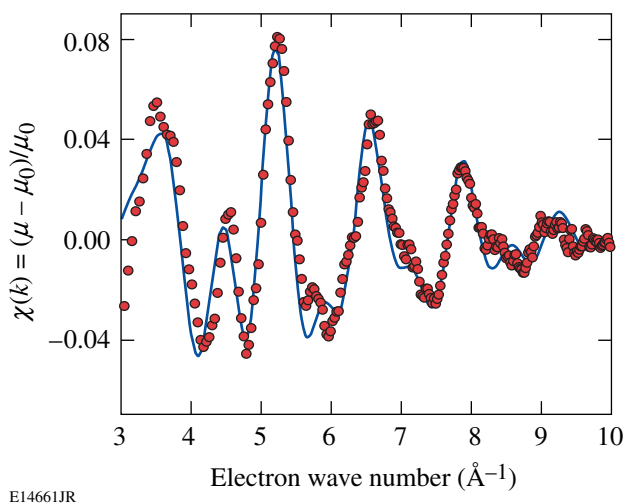

E14661JR

Figure 111.38
Fitting spectra calculated by the FEFF code to the measured EXAFS for the case where the drive beams were not shot. The temperature of the best-fit spectrum corresponds to an increase above room temperature of $\Delta T \sim 200$ K. This heating is due to radiation from the imploding spherical target. The density of the best-fit spectrum corresponds to the normal density of vanadium.
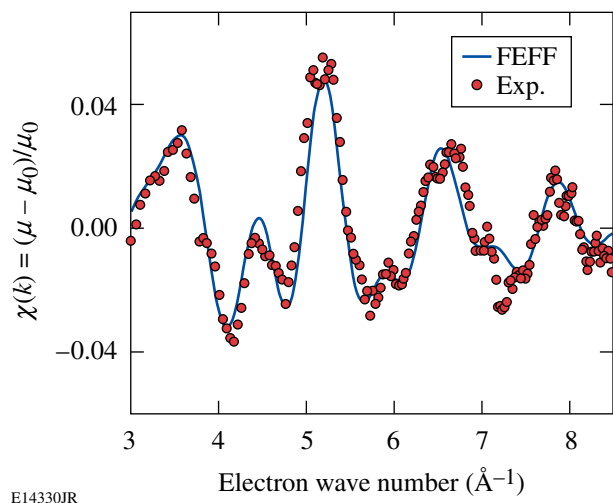
E14330JR

Figure 111.39
Fitting FEFF spectra to the measured EXAFS of a driven target at 20 ns (i.e., before the impact of the expanding reservoir on the vanadium sample). This serves to determine the preheat due to radiation from the laser-deposition region, 130 K in this case.

the laser intensity required for achieving the same pressure is about ten times smaller than in the case of ICE. Nevertheless, the heating due to compression alone is considerably lower in the case of ICE.

5. EXAFS Measurement of Compression and Temperature
    EXAFS measurements of the vanadium were made around peak compression. Figure 111.40 shows the raw measured spectra for undriven and driven ICE vanadium targets [(before extracting the $\chi(k)$ function]. In the undriven case only the backlighter target was irradiated; the driven case refers to a target with a heat shield, a 300-μm vacuum gap, irradiated at 17 TW/cm^2. Comparison of the EXAFS modulations above the vanadium K edge for the two spectra clearly shows the effect of compression: (a) a higher density, as evidenced by the lengthening of the EXAFS modulation period, and (b) heating, as evidenced by the faster damping of the oscillations with increasing photon energy. The driven spectrum of Fig. 111.40 was analyzed with the FEFF EXAFS code. The best fit, shown in Fig. 111.41, yields the conditions within the vanadium at the time 39 ns (with respect to firing the drive-laser beams). The best fit corresponds to a compression of 15% (i.e., a density of 7 g/cm^3) and a temperature of 720 K.

    As explained in the **Introduction** (p. 167), the FEFF fit yields the parameters R and σ^2; R (the nearest-neighbor distance) yields the density, whereas the temperature is derived
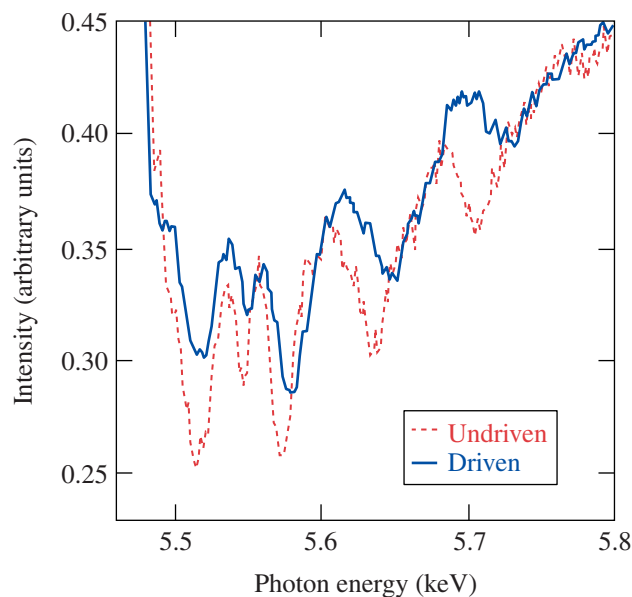

E15770JR

Figure 111.40
Measured spectra for undriven and driven ICE vanadium targets (before extracting the χ function). Comparison of the EXAFS modulations above the vanadium K edge for the two spectra clearly shows the effect of compression, namely, the lengthening of the modulation period, and the effect of heating, namely, the faster damping with increasing photon energy.
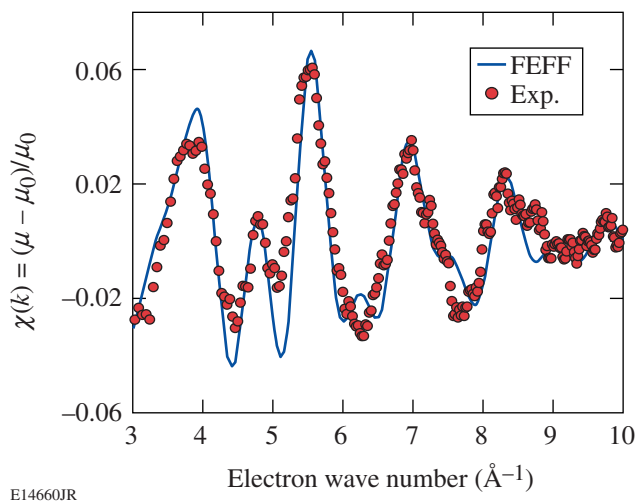

E14660JR

Figure 111.41
EXAFS measurement of ICE compression: fitting FEFF spectrum to the measured EXAFS for the case of an ICE target irradiation at ~17 TW/cm^2. The fitting parameters yield a compression of 15% and a temperature of 720 K. Only ~90 K is the increase due to compression; the rest is preheat. This is a demonstration that laser-driven ICE can achieve a similar compression at a lower temperature than in shock compression.

from σ^2 and the density. The corresponding *LASNEX* simulation of the vanadium density for a 300-μm-vacuum-gap target, with heat shield, at 39 ns is shown in Fig. 111.42, showing a uniform profile. The time 39 ns [which is slightly past peak compression, see Fig. 111.36(a)] was chosen because then the compression profile becomes uniform. The measured compression value is in excellent agreement with *LASNEX*. As seen above, of the total temperature rise from room temperature, $\Delta T \sim 200$ K is the increase due to radiation from the backlighter and $\Delta T \sim 130$ K is the increase due to radiation from the laser-absorption region. Thus, only ~90 K is the increase due to compression. This result can be compared with the EXAFS measurement of shock compression of vanadium,[8] where the same compression was accompanied by a temperature rise of $\Delta T = 770$ K. Thus, *laser-driven ICE can achieve a similar compression at a lower temperature than in shock compression*. At higher drive pressures this advantage of ICE will increase because although preheat by radiation from the laser-absorption region will be higher, the main preheat (due to the backlighter) need not increase.
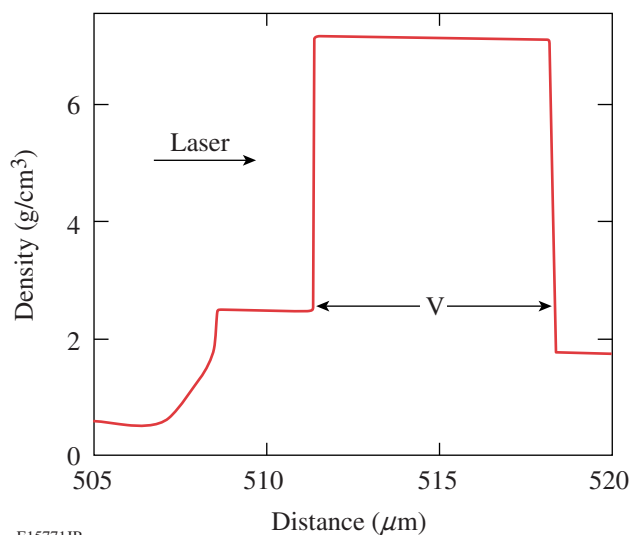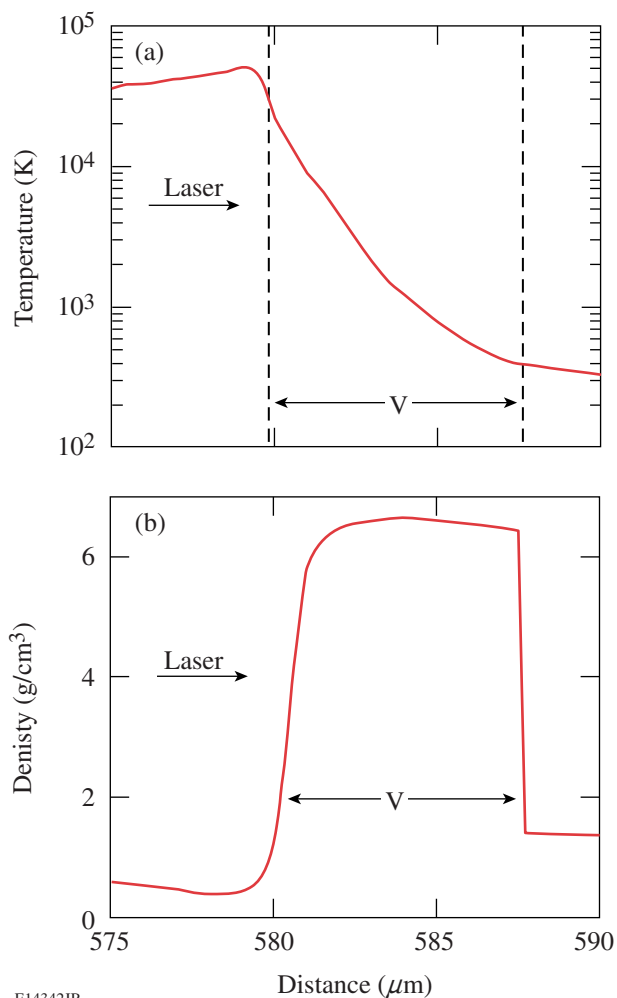

Figure 111.42
LASNEX simulation of the vanadium (V) density for a target with a heat shield, 300-μm vacuum gap, at 39 ns. By the time the pressure starts to fall the density becomes uniform. The density (~7 g/cm^3) corresponds to a compression of 1.15, in very good agreement with the measured value (Fig. 111.4l).

We turn now to the case of an ICE target without a heat shield. As discussed above, the severe heating of the vanadium front surface creates a strong temperature gradient that makes the EXAFS analysis more complicated and less reliable. The value of such target shots is mostly in demonstrating that without a heat shield such severe heating indeed takes place. Fig-

ure 111.43 shows the relevant *LASNEX*-simulated temperature and density profiles for a 400-μm-vacuum-gap target without a heat shield, at 37 ns. Heating from the plasma impact is seen to be severe. The density profile shows, as explained above, a lower density than in the case of a target with a heat shield (Fig. 111.42): ~6.5 g/cm^3 (compression of 8%) as compared with ~7 g/cm^3 (compression of 15%). We use these profiles to calculate the expected EXAFS spectra, shown in Fig. 111.44(a). For various depths within the vanadium, EXAFS spectra are calculated by the FEFF code, using the local density and temperature values given by *LASNEX*. Three examples of such spectra are shown, as well as the spatial average. The

Figure 111.43
LASNEX-simulated temperature (a) and density (b) profiles for a 400-μm-vacuum-gap target without a heat shield, at 37 ns. Heating from the plasma impact is seen to be severe, resulting in a lower density (or compression). The profiles are used to calculate the expected EXAFS spectrum [Fig. 111.44(a)] by averaging over the spatially resolved EXAFS spectra.

regions of higher temperatures contribute very little to the average. Effectively, the average is over the region where the temperature is less than ~1000 K. The main effect of the high temperature is to lower the amplitude of the average spectrum. This is because the secular absorption $\mu_0(k)$, appearing in the denominator of $\chi(k)$, is independent of temperature and thus corresponds to absorption throughout the vanadium thickness. Since the amplitude of the average spectrum in Fig. 111.44(a) is smaller than that in Fig. 111.41 (the case with a heat shield) by a factor of ~2.5, the front ~60% of the vanadium thickness has temperatures much higher than ~1000 K; this agrees with the computed temperature profile in Fig. 111.43(a). Thus, *the impact heating and its suppression by the heat shield is demonstrated*. Figure 111.44(b) shows a comparison of the average spectrum from (a) and the corresponding experimental spectrum. Unlike in Figs. 111.38, 111.39, and 111.41 where FEFF profiles were adjusted to fit the data, here the FEFF profiles are fixed by the *LASNEX*-calculated parameters.

However, some adjustment had to be made in the frequency of the calculated EXAFS (adding 4% compression) to fit the data, but, even so, the fit is poor. This is due to the difficulty in correctly simulating EXAFS in a steep temperature gradient. Nevertheless, the main goal of such target shots was realized: the low amplitude of the spectrum in Fig. 111.44(b) as com-

pared with that in Fig. 111.41 is clear evidence of significant sample heating when a heat shield is not used.

Conclusions

In summary, EXAFS measurements in isentropic compression experiments show details not accessible by VISAR measurements. In particular, the sample temperature has been measured. To determine the temperature rise due to the compression, the preheat was determined separately and subtracted out. This preheat is due to three sources: radiation from the laser-deposition region, radiation from the backlighter, and heat conduction from the front surface of the target. In the present experiment the preheat was higher than the heating due to the compression. In future experiments at higher compressions, however, the reverse may be true. The experiments showed that when a heat shield is not present, significant heating occurs within a few microns of the surface. The shock generated by the heat shield has only a small effect on the main compression wave; a heat shield made of a material of high sound speed (such as diamond) may greatly reduce this shock. The experiments also showed that a nonuniform compression occurs at irradiances higher than ~20 TW/cm^2 (or pressures higher than ~0.6 Mbar); the more-uniform irradiation of a hohlraum excited by the laser beams may reduce this effect.
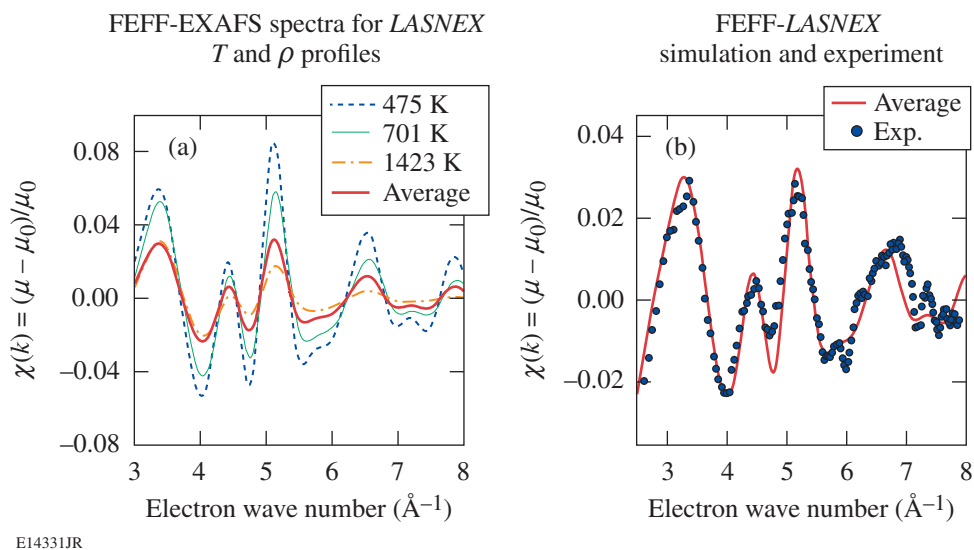
E14331JR

Figure 111.44
EXAFS analysis for the nonuniform case of an ICE target without a heat shield. (a) For various depths within the vanadium, EXAFS spectra are calculated by the FEFF code, for the density and temperature values given by *LASNEX* (Fig. 111.43). Three examples of such spectra are shown, as well as the spatial average. (b) Comparison of the average spectrum from (a), with slight adjustments, and the corresponding experimental spectrum. The low amplitude of the spectrum in Fig. 111.44(b) as compared with that in Fig. 111.41 is evidence for significant sample heating when a heat shield is not used.

REFERENCES

1. B. A. Remington, G. Bazan, J. Belak, E. Bringa, M. Caturla, J. D. Colvin, M. J. Edwards, S. G. Glendinning, D. S. Ivanov, B. Kad, D. H. Kalantar, M. Kumar, B. F. Lasinski, K. T. Lorenz, J. M. McNaney, D. D. Meyerhofer, M. A. Meyers, S. M. Pollaine, D. Rowley, M. Schneider, J. S. Stölken, J. S. Wark, S. V. Weber, W. G. Wolfer, B. Yaakobi, and L. V. Zhigilei, Metall. Mater. Trans. A **35A**, 2587 (2004).

2. T. R. Boehly, R. S. Craxton, T. H. Hinterman, J. H. Kelly, T. J. Kessler, S. A. Kumpan, S. A. Letzring, R. L. McCrory, S. F. B. Morse, W. Seka, S. Skupsky, J. M. Soures, and C. P. Verdon, Rev. Sci. Instrum. **66**, 508 (1995).

3. P. A. Lee *et al.*, Rev. Mod. Phys. **53**, 769 (1981).

4. C. Dai *et al.*, J. Phys. D: Appl. Phys. **34**, 3064 (2001).

5. J. Edwards *et al.*, Phys. Rev. Lett. **92**, 075002 (2004).

6. K. T. Lorenz *et al.*, Phys. Plasmas **12**, 056309 (2005).

7. K. T. Lorenz *et al.*, High Energy Density Phys. **2**, 113 (2006).

8. R. F. Smith *et al.*, Astrophys. Space Sci. **307**, 269 (2007).

9. B. Yaakobi, D. D. Meyerhofer, T. R. Boehly, J. J. Rehr, B. A. Remington, P. G. Allen, S. M. Pollaine, and R. C. Albers, Phys. Plasmas **11**, 2688 (2004).

10. B. Yaakobi, T. R. Boehly, D. D. Meyerhofer, T. J. B. Collins, B. A. Remington, P. G. Allen, S. M. Pollaine, H. E. Lorenzana, and J. H. Eggert, Phys. Plasmas **12**, 092703 (2005).

11. J. J. Rehr, R. C. Albers, and S. I. Zabinsky, Phys. Rev. Lett. **69**, 3397 (1992).

12. E. Sevillano, H. Meuth, and J. J. Rehr, Phys. Rev. B **20**, 4908 (1979).

13. R. M. More *et al.*, Phys. Fluids **31**, 3059 (1988).

14. G. R. Gathers, J. Appl. Phys. **59**, 3291 (1986).

15. G. J. Streletz and L. H. MacFarland, in *Shock Compression of Condensed Matter–1999*, edited by M. D. Furnish, L. C. Chhabildas, and R. S. Hixson, AIP Conf. Proc. 505 (American Institute of Physics, New York, 2000), pp. 201–204.

16. P. M. Celliers *et al.*, Appl. Phys. Lett. **73**, 1320 (1998).

17. D. B. Hayes, Sandia National Laboratory, Albuquerque, NM, SAND2001-1440, NTIS Order No. DE2001-783087 (2001); D. B. Hayes *et al.*, J. Appl. Phys. **96**, 5520 (2004).

18. G. B. Zimmerman and W. L. Kruer, Comments Plasma Phys. Control. Fusion **2**, 51 (1975).

19. T. J. Kessler, Y. Lin, J. J. Armstrong, and B. Velazquez, in *Laser Coherence Control: Technology and Applications*, edited by H. T. Powell and T. J. Kessler (SPIE, Bellingham, WA, 1993), Vol. 1870, pp. 95–104.

20. J. G. Wouchuk and R. Carretero, Phys. Plasmas **10**, 4237 (2003).